Polarized neutron imaging and three-dimensional calculation of magnetic flux trapping in bulk of superconductors

Wolfgang Treimer,[1,2,*] Omid Ebrahimi,[1,2] Nursel Karakas,[1,2] and Ruslan Prozorov[3]

[1]*Beuth Hochschule für Technik Berlin, Department of Mathematics, Physics and Chemistry, D-13353 Berlin, Germany*

[2]*Helmholtz Zentrum für Materialien und Energie Berlin, Joint Department G-G1, D-14109 Berlin, Germany*

[3]*Ames Laboratory and Department of Physics and Astronomy, Iowa State University, Ames, Iowa 50011, USA*

(Received 20 December 2011; revised manuscript received 29 March 2012; published 17 May 2012)

Polarized neutron radiography was used to study the three-dimensional magnetic flux distribution inside of single-crystal and polycrystalline Pb cylinders with large (cm^3) volume and virtually zero demagnetization. Experiments with single crystals being in the Meissner phase ($T < T_c$) showed the expected expulsion of magnetic field. 99.9999 wt % pure polycrystalline samples were exposed to the same homogeneous magnetic field (6.4 mT) and only a portion of the applied field was expelled. The trapped field in the sample ($T < T_c$, $B_{ext} = 0$ T) showed a nearly Gaussian spatial distribution, centered on the cylinder axis and decreasing towards the surface of the cylinder. In the direction along the cylinder axis the trapped flux was nearly constant. The expelled field outside of the samples followed $1/R$ dependence. These measurements provided a unique and detailed picture of macroscopic superconducting samples, confirming the existence of both uniform bulk Meissner expulsion in single crystals and bulk flux trapping with nearly-Bean-model profiles due to flux pinning in polycrystalline samples.

DOI: 10.1103/PhysRevB.85.184522 PACS number(s): 74.20.−z, 74.25.Ha, 28.20.Pr

I. INTRODUCTION

The physics of flux trapping in superconductors is of principle interest due to the lack of a uniform theory describing amount, shape, and distribution of trapped magnetic fields and because trapped magnetic fields in superconducting devices often cause significant reduction in efficiency. The appearance of an intermediate state in type I superconductors is of great interest due to its connection to a variety of phenomena dealing with pattern formation and questions of thermodynamic equilibrium in finite systems where the laws of thermodynamics are not directly applicable. The intermediate state appears due to demagnetization effects when the magnetic field on the sample edge exceeds the critical field, H_c, but the external applied field is still less than H_c. Due to positive surface energy between the superconducting and normal phases, rich patterns of the magnetic flux can be formed in order to minimize the total free energy. In addition, magnetic flux needs to redistribute and move within the sample when the magnetic field is increased or decreased and additional requirements of the topological mobility must be considered. The simplest static solution was proposed by Landau[1] and was the subject of numerous investigations afterward. In his paper, Landau stated that a body in the intermediate state consists of alternating layers of the superconducting and the normal phase, and that their thicknesses are greatest in the inner part of the body. An experimental proof was provided, utilizing a lead sample which was disk-shaped[2] (the diameter was 9 mm and the thickness 3 mm; this geometry came closest to our samples which were 12 mm in diameter and 30 mm in length). The Landau solution—a stripe phase in the one-dimensional case or more generally a laminar phase in the two-dimensional (2D) case—was later extended and modified to try to match the growing number of experimental inconsistencies, most notably the observation of flux tubes in the earliest experiments by Meshkovsky and Shalnikov.[3,4] There have been a great many papers dealing with experimental investigations of the intermediate state. It is now obvious that measurements of magnetization or resistivity taken without knowledge of the flux pattern should be considered questionable, because a complex interplay of the flux structure and flux pinning make it almost impossible to model the system. Other measurements have focused on visualization of the flux patterns and this is a subject of our interest here. As stated above, the intermediate state is observed for samples with sufficient demagnetization factor N (Refs. 5 and 6) existing in the interval $H_c(1 - N) < H_{appl} < H_c$. However, flux pinning causes inhomogeneous distribution of flux for any geometry. Moreover, the experiments so far have only been able to visualize the flux on the sample surface, thus leaving the interior subject to various speculations, such as flux branching.[7,8] In Ref. 8, the observations were done by decoration with small iron particles, a rather rough method compared to modern magneto-optical imaging methods. Nonetheless, these images displayed signatures of complicated intermediate-state structures, observed later by magneto-optical methods which have revealed a rich variety of patterns.[9] These early publications dealing with flux pinning and intermediate state gave the first hints that the physical problems to be solved may have no simple solutions. The corresponding thermodynamics of metastable processes in the magnetization of type I superconductors was also investigated in detail in Ref. 10. However, as was calculated and summarized in Refs. 11 and 12, the main problem was to predict the pattern of penetration in objects in the magnetic intermediate state. More recent works with high-resolution magneto-optics have tried to separate effects of intrinsic (“topological”) hysteresis and the hysteresis caused by flux pinning.[13–21] The main focus of these publications was distinguishing between two distinct topologies of the intermediate state in type I superconductors: One topology is continuous and closed under the formation of flux tubes in the presence of external penetrating fields, and the second is an open and discontinuous topology in the absence of external fields which allows trapped flux to

migrate to the edges through the produced laminar pattern. In the progress of these investigations a unique phase, named "suprafroth" was identified and shown to obey statistical laws governing the behavior of other froths.[22] With applied magnetic field, flux structures may be tuned and imaged with a magneto-optical imaging technique and from these images flux pinning in the bulk of the samples may be observed and explained. Several publications describe and calculate a geometry-dependent magnetic energy barrier and report that the magnetization of type I superconductors samples showed an irreversible behavior,[11,12,21] assuming a migration of flux tubes toward the center of the sample. Recent calculations concerning confinement effects on intermediate-state flux patterns in mesoscopic type I superconductors predict tubular and laminar structures, and that they are strongly influenced by the geometry of the sample. For a local visualization of asymmetric flux pinning in superconducting Pb films the field polarity dependence of flux pinning was used;[13] however, the volumes under investigation were extremely small ($\ll 1$ mm^3), and these results may not be extrapolated to fit samples three orders of magnitude larger. Moreover, in early works it was stated that due to the Gibbs free-energy barrier, the critical magnetic field for entry magnetic flux depends on the square root of the width of a cylinder.[23] The intermediate state revealed phenomena that were not predicted by the first theories[1] and experiments are still necessary to better understand flux pinning in type I superconductors.[24] Despite the high resolution of magneto-optical imaging, the technique remains two-dimensional, only revealing the physics of the sample surface. Thus any conclusions drawn from it remain under the shadow of "surface-only" phenomena. Additionally, as mentioned above, up to now all theoretical and experimental research work on the intermediate state of type I superconductors was done with samples that had rather two-dimensional shape and relatively small size.

This paper presents magnetic field distributions inside and outside of cm^3-large, massive lead samples in the Meissner phase and intermediate state measured with polarized neutrons. To separate pure Meissner response from the effects of bulk pinning, our samples were long cylinders having virtually no demagnetization. The obtained results are unambiguous and leave no room for other interpretations.

II. THEORY

From quantum mechanics it is well known that the spin $S = S(t)$ behaves in a magnetic field B as

$$\dot{S}_j(t) = \frac{\mu_N}{h} g[\vec{S}(t) \times \vec{B}(t)]_j \quad j = x,y,z. \tag{1}$$

$\mu_N = 5.050\,783\,43 \times 10^{-27}$ [J/T] is the nuclear magneton and $g = -3.826\,085$ the Landé factor for neutrons, $h = 6.626\,075\,5 \times 10^{-34}$ [J s], $\hbar = h/2\pi$. The motion of the spin of a low-energy neutron can be described as being like a classical magnetic moment having a Larmor frequency $\omega_L = \gamma_L \cdot B$. γ_L is the gyromagnetic ratio of the neutron, $\gamma_L = g \cdot \mu_N/\hbar = -1.832\,47 \times 10^8$ rad s^{-1} T^{-1}. Therefore the angle of rotation ϕ is given by $\omega_L \cdot t$, t = time the spin moves in the magnetic field B; thus the number of spin rotations is given finally by the path integral

$$\phi = \omega_L \cdot t = \gamma_L \cdot B \cdot t = \frac{\gamma_L}{v} \int B \cdot ds = \frac{\gamma_L \cdot m}{h} B \cdot s \cdot \lambda. \tag{2}$$

v = velocity of the neutron, B = magnetic field, m = neutron mass, s = path length in the field, λ = wavelength, and h = Planck's constant. For a mean neutron wavelength $0.39.10^{-9}$ m the velocity $v = h/(m.\lambda) = 1014$ m s^{-1}. The spin of a monochromatic neutron beam passing through an inhomogeneous magnetic field will experience different Larmor precessions ω_L depending on the path integral $\int B(x,y,z)ds$. The registered intensities $I = I(x,y,z)$ depend on the incident intensity I_0, on the attenuation due to the sample, and on the spin orientation in front of the spin analyzer. Involving the different transmission factors of the spin polarizer, collimators, and spin analyzer that attenuate the beam, combined with the factor T, the intensity measured with a 2D detector as $I(x,z)$ and $I(y,z)$, respectively, can be written for two perpendicular sample orientations (cf. Fig. 1) as

$$I(x,z) = \underbrace{I_0(x,z) \cdot T \cdot \exp\left[-\int_{\text{path}} \Sigma(s)ds\right]}_{I_{\text{att}}(x,z)} \cdot \underbrace{\frac{1}{2}[1+\cos\phi(x,z)]}_{I_{\text{spin}}(x,z)},$$
$$I(y,z) = \underbrace{I_0(y,z) \cdot T \cdot \exp\left[-\int_{\text{path}} \Sigma(s)ds\right]}_{I_{\text{att}}(y,z)} \cdot \underbrace{\frac{1}{2}[1+\cos\phi(y,z)]}_{I_{\text{spin}}(y,z)}. \tag{3}$$

I_{att} is the amplitude of an oscillating cosine function and Σ is the linear attenuation coefficient of the sample. The factor $T < 1$ involves all the other intensity I_0 reducing parts as mentioned above. I_{spin} describes the intensity oscillations due to spin rotation in B. To calculate I_{spin} one has to determine all possible paths of neutron spins through the sample and calculate $\int B \cdot ds$. These path integrals were calculated using only one projection of the Radon transform $R\{f\}$ for one angle α, only as[1]

$$R_{0,\alpha=\text{const}}\{f\} = \hat{f}_0(p,\alpha) = \int_{-\infty}^{\infty}\int_{-\infty}^{\infty} B(x,z) \cdot \delta[p - x \cdot \cos(\alpha) - z \cdot \sin(\alpha)] \cdot dx \cdot dz,$$
$$R_{90,\alpha=\text{const}}\{f\} = \hat{f}_{90}(p,\alpha) = \int_{-\infty}^{\infty}\int_{-\infty}^{\infty} B(y,z) \cdot \delta[p - y \cdot \cos(\alpha) - z \cdot \sin(\alpha)] \cdot dy \cdot dz. \tag{4}$$

p is the scanning variable over the 2D function f. R_0 and R_{90} are the Radon transforms for the sample orientations 0° (parallel to the neutron beam) and 90° (perpendicular to the neutron beam; cf. Figs. 1 and 8 for a cylindrical sample). From Eq. (4) $B(x,y,z)$ can be calculated if the corresponding Radon transforms are known, i.e., if they can be measured. A

[1]The sample in the cryostat was found to be misaligned about 4°; therefore the angle α was varied about $\pm 4°$ in order to fit the theoretical orientation to the sample.

depolarization of the neutron spin is produced if the neutrons pass through fields trapped in or around superconductors that are in the Meissner phase or intermediate state. Therefore a 2D projection image of this volume shall give information about the amount and shape of the trapped field.

The first image of a magnetic field of a small magnet was realized already in 1997, and published later.[25] Neutron radiography and tomography with polarized neutrons became more prominent after that with improved instrumentation and the possibility of new experiments.[26,27] In neutron scattering the technique of neutron spin rotation and spin analysis is well established. Therefore this method is extreme suitably for the investigation of magnetic fields in bulk materials as was shown in the last few years.[28–30]

III. EXPERIMENTAL SETUP AND COIL EXPERIMENT

The experiments were performed at the research reactor BER II of the Helmholtz Zentrum Berlin.

In order to observe the Meissner effect and flux pinning (flux trapping) in the different lead samples we used the instrument PONTO (polarized neutron tomography) at the BER II reactor of the Helmholtz Centre for Materials and Energy, Berlin. This instrument is dedicated to radiography and tomography with polarized neutrons and already described in detail in Ref. 31.

PONTO is situated at the Nl1b neutron guide in the guide hall of the BER II research reactor. The experimental layout is shown in Fig. 1. A graphite monochromator (002) reflected a mean neutron wavelength of 0.39(1) nm to the optical bench; a horizontal and a vertical collimator (0.1°, 0.2°) and a spin polarizer[32] prepared the neutron beam with

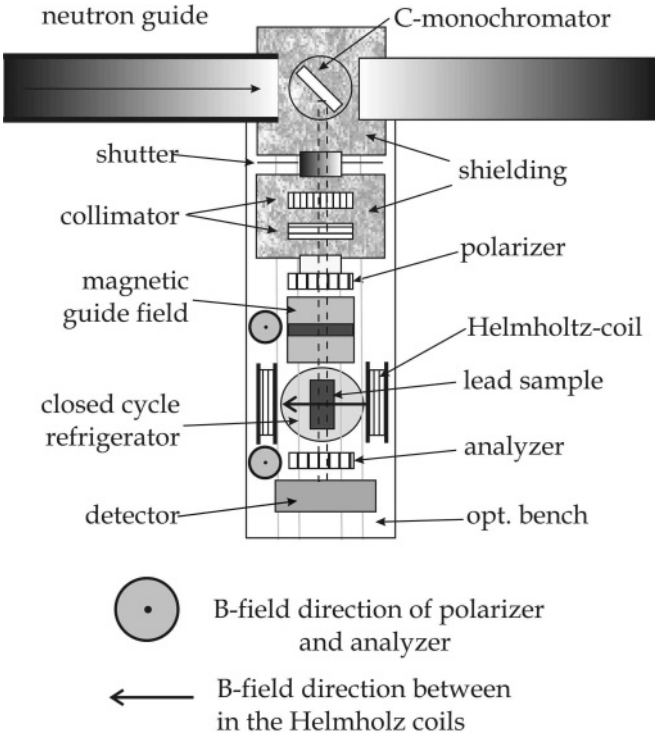

FIG. 1. Sketch of the experimental layout (instrument PONTO); objects in the figure are not scaled to each other.

respect to collimation (direction) and spin state ("up"). Here "spin up" means that the direction of the neutron spins was perpendicular to the plane of the optical bench, i.e., parallel to the magnetic guide field (see Fig. 1). In order to image the magnetic field outside and inside the samples we used the fact that the orientation of the neutron spin is influenced by the magnetic field if the spin is not parallel to the incident B orientation. Therefore a guide field B_{guide} (1.7 mT) after the spin polarizer (first bender) kept the spin in its given orientation ("spin up") until the neutrons enter the magnetic field B_{Helm} of the Helmholtz coils (6.4 mT) and the sample (crystal, polycrystalline) in the cryostat. The spin orientation was measured with the analyzer (second bender), which was placed close to the 2D detector. The guide field B_{guide} and the Helmholtz field B_{Helm} were ∼170 mm apart from (and perpendicular to) each other in order to minimize the overlap of stray fields. The guide field B_{guide} decreased ∼<20 mm downstream in front of the Helmholtz field B_{Helm} to 0.3 mT in such a way that entering in B_{Helm} an adiabatic transition of the neutron spin was very unlikely.

The overall polarization of the neutron beam was measured to 85(3)%. The samples were kept in a special Al holder (Fig. 4) and cooled with cryostat stepwise to 5.5 K keeping the temperature constant again for 3 h. An external homogeneous magnetic field $B_{\text{ext}} = 6.4$ mT (Helmholtz coils) was constantly applied perpendicular and parallel to the cylinder axis if the Meissner state was investigated. The sample temperature was raised in different steps (5.5, 6.8, 7.0, 7.4 K) up to 8 K. At each temperature images were recorded after a waiting time of 3 h, to guarantee a constant temperature all over the sample (a COMSOL simulation of the cooling time yielded ∼2 min to reach the temperature). The images were registered with a CCD camera (1 k × 1 k, pixel size = 43 μm) and the images were processed as follows: All images were filtered with a median filter (2 × 2) to get rid of hot spots, dark- and flat-field corrected, and then normalized to images measured at 7.4 and 8.0 K, respectively. The experiments were steered with a LABVIEW program, controlling measuring time, temperature, step motors, spin rotation coils, Helmholtz coils, detector unit, etc.

The used incident neutron beam (monochromatic, wavelength 0.39 nm, horizontal divergence 0.2°, vertical divergence 0.1°), was polarized and spin analyzed with so-called benders.[32,33] The polarization state of the neutron beam was the most crucial part of all studies. The overall polarization P of the instrument was measured several times using the shim method and spin rotation method.[31] With the shim method the transmitted depolarized beam was measured after a "shim plate" of iron was put in the polarized beam in front of the analyzer, destroying the spin orientation. The ratio of the transmitted intensity—with and without shim plate, each reduced by the background—yields the polarization P as $P = \{\frac{I_{\text{pol}} - I_{\text{background}}}{I_{\text{depol}} - I_{\text{background}}} - 1\} \times 100$.

The second method used the rotation of the neutron spin in a magnetic field which is not parallel to the spin direction. Then the spin rotates around B with the Larmor frequency and causes intensity variations behind the analyzer between 0% and 100% if the beam is 100% polarized. Both methods yielded a $P = 85(3)\%$.

The distance between sample and spin analyzer had to be ∼200 mm to keep the influence of the stray fields of the analyzer less than 0.05 mT. This was measured with a Hall probe yielding a $5 \times 5 \times 5$ matrix, each voxel being a small cube of $5 \times 5 \times 50$ mm^3. With a spin rotation unit in front (upstream) of the sample the incident spin orientation could be changed continuously from parallel to antiparallel (from spin "up" to spin "down"). Measurements with spin flips from up to down (and vice versa) guaranteed that the observations were pure magnetic nature, because nothing else was changed in the experimental setup. Thus we knew exactly the "magnetic path" of the neutron spins beginning from the polarizer until the spin analyzer and the 2D detector. The field of view (FOV) of both spin polarizer and analyzer was not perfectly homogeneous; however, using them for all experiments, unchanged in their position, all images could be corrected with "dark and flat images," i.e., images without the sample and with the sample having a temperature T = 7.4 or 8 K, suppressing inherent structures. This was controlled before and after each experiment.

The main purpose of our experiment was to visualize both expelled and trapped magnetic fields of samples in the Meissner as well as the intermediate state. The magnetic field of a Cu coil was first imaged using our technique as a form of calibration. In order to image the magnetic field in the coil the same method was used as we described above. A polarized neutron beam interacts with a magnetic field in such a way that the neutron spin rotates around B with the Larmor frequency ω_L and the angle of rotation depends on B and on the path length in B, only (see "Theory," Fig. 3). The spin state of a neutron beam after interacting with any magnetic field distribution can be analyzed with respect to its initial spin state with a spin analyzer in front of the 2D detector. In the case of a simple coil the neutron spin interacts with a uniform field which has a cylindrical shape, as shown in Fig. 2, and the image can be easily calculated and measured with polarized neutrons.

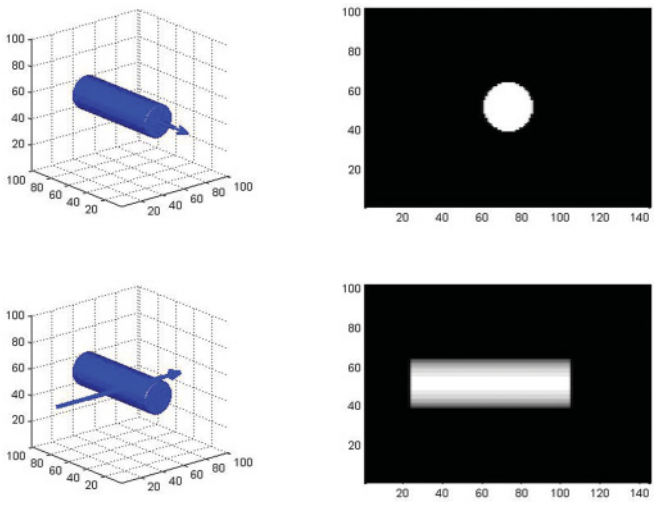

FIG. 2. (Color online) Orientation of the coil and beam. The magnetic field of a coil can be represented as a homogeneous (long) cylinder; left part shows orientation of the coil with respect to the neutron flight direction (arrow); right images are the corresponding projections of the coil.

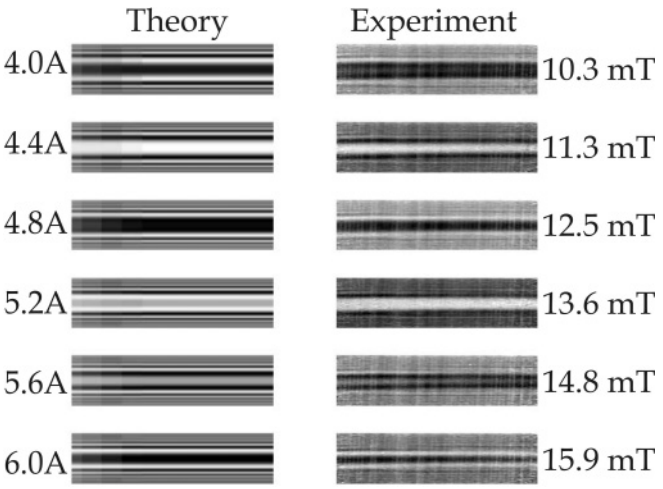

FIG. 3. Comparison of theory with experimental data. 4–6 A currents yield a magnetic flux $B = 10.3$ mT to 15.9 mT: Calculated and measured fringe pattern due to position-dependent depolarization of the neutron spin in a coil. The agreement of the experimental data with the calculated ones underlines both the presence of a uniform magnetic field and the sensitivity of the imaging technique (image height =22 mm).

If the coil axis is horizontally perpendicular to the incident neutron beam direction the path length through the cylinder depends only on the height (z value) of the beam, and is at most $2R$ if it passes through the middle of the cylinder. Thus the magnetic field of a (Cu) coil having a diameter of 22 mm, a length of 90 mm, and 205 windings was imaged by increasing the current from 4 up to 6 A, which caused an increasing uniform magnetic field in the coil. Due to the circular cross section of the coil one expects a fringe pattern as shown in the left column ("Theory"); the experimental results are given in the right column ("Experiment") in Fig. 3, both indicating a homogeneous magnetic field in the coil.

IV. SAMPLES

Similar behavior is expected in the intermediate state for both the ⟨110⟩ oriented lead cylinder single crystals and the polycrystalline samples with trapped flux. The cylindrically shaped lead samples (all 12 mm diameter, 300 mm height) were bought from MaTecK GmbH, Gemany, and analyzed for accuracy of stated purity in house. The single crystal (⟨110⟩ rod orientation) consisted of the isotopes 24% Pb^{206}, 23% Pb^{207}, and ⩽53% Pb^{208}; all other elements were <1 ppm. The mosaic spread (1.76°) was determined independently using the ultra-small-angle neutron scattering (USANS) instrument V12 at the BER II reactor.[34] The purity of the polycrystalline lead crystal was given by MaTecK to 99.9999 wt %.

The samples (∼200 mm apart from the detector) were kept in a special Al holder (Fig. 4) and cooled with a conventional cryostat which was placed in a homogeneous horizontal magnetic field $B_{\text{ext}} = 6.4(1)$ mT generated with two Helmholtz coils (diameter 200 mm). The cooling from 300 down to 8 K could be done within 2 h (134 min). After reaching 8 K so-called dark and flat images (radiographs) were measured, which were used to normalize all images.

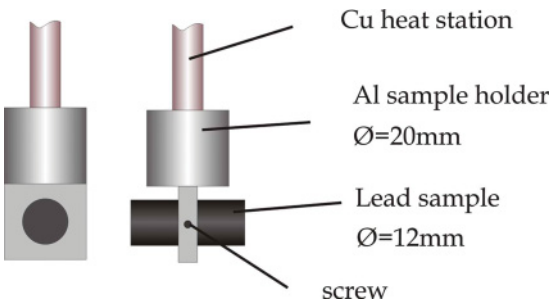

FIG. 4. (Color online) Al sample holder with lead cylinder. Lead sample (dark gray) is fixed with an Al sample holder to the Cu cooling (heat) station.

Then the samples were cooled down from 8 to 5.5 K in incremental time steps of 3 h. Temperature steps used were 7.4, 6.8, 6.0, and 5.5 K. Each sample reached homogeneous temperatures at each plateau in ∼120 min, where it then remained for the duration of each measurement. All experiments for the Meissner phase were performed with the external magnetic field of 6.4 mT, i.e., the field was switched on all the time (during cooling and measurement). The sample was imaged for two axis orientations, one perpendicular and the other parallel to the neutron flight direction. In the case of the flux pinning measurements the sample was cooled down to 5.5 K; then the field was switched off and the sample rotated.

V. POLARIZED NEUTRON IMAGING

A. Single-crystal sample

For lead single crystals trapped flux should not occur, only the Meissner effect. First, the sample axis was perpendicular to the external magnetic field (and parallel to the neutron flight direction). The neutron spin was "up" // to B_{ext}. The images (see Fig. 5) were normalized to the image at $T = 8$ K to visualize the magnetic interaction. As can be seen, around the sample dark fringes appear if $T < T_c$ and vanish for $T > T_c$. Due to a small misalignment of the sample in the cryostat the fringes seem to appear also inside the sample, but inside the sample no magnetic fields could be observed (cf. Fig. 6). If the sample temperature was raised above T_c up to 7.4 K the fringes disappear.

The sample was then rotated by 90° such that the rod axis was parallel to the B_{ext} and perpendicular to the neutron

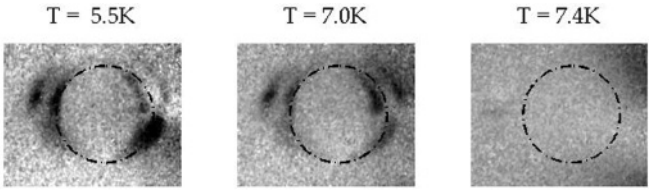

FIG. 5. Meissner phase, sample orientation 90°. Observation of the Meissner effect with a lead ⟨110⟩ single crystal, $B_{\text{ext}} = 6.4$ mT; black circles (projection diameter =12.7 mm) indicate the sample, orientation of B_{ext} perpendicular to the rod axis; cf. Fig. 1. Black fringes around the sample are due to spin depolarization caused by the expelled field. For $T = 7.4$ K $> T_c$ fringes disappear.

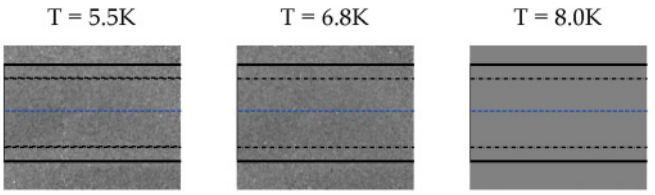

FIG. 6. (Color online) $B_{\text{ext}} = 0$, sample orientation 0°. No flux pinning was observed in the lead single crystal; black lines indicate the height of the sample (projection diameter =12.7 mm); blue line is the rod axis. Images were normalized to $T = 8$ K.

flight direction. Switching off the magnetic field one could not observe any flux pinning in the lead single crystal (Fig. 6).

Both series of neutron radiographs proved that the sample being the Meissner phase expelled the magnetic field appreciably. Any trapped field would be observed in the imaging as differences above and below T_c; no significant differences are observed in Fig. 6.

B. Polycrystalline lead sample

The investigations of the pure polycrystalline sample were much more surprising. All lead samples had the same size and shape and were investigated in the same manner. The polycrystalline samples were cooled in the same manner as the single crystals; the series radiographies were repeated for the Meissner phase and possible intermediate state. Again the lead cylinder was imaged in positions orientated parallel and perpendicular to the neutron flight direction (cf. Fig. 1). We started with the sample orientation ⊥ to $B_{\text{ext}} = 6.4$ mT and cooled the sample down as described above for the single-crystal sample. Again at $T = 8$ K dark and flat images were taken before the sample was cooled down to $T = 5.5$ K. After a waiting time >3 h neutron spin-resolved 2D radiographs were recorded with $B_{\text{ext}} = 6.4$ mT; Fig. 7 shows the result.

One sees fringe patterns in the images $T = 6.2$ K and $T = 7.0$ K and they seemed to extend into sample; however, the precise adjustment of the sample together with the large cryostat parallel (perpendicular) to the neutron beam better than ±4° was quite difficult to realize; hence the cylinder was horizontally misaligned about 4(1)°. The expelled magnetic field was also horizontally misaligned thus changing its shape and projection with respect to the polarized neutron beam; large dark areas in the images $T = 6.2$ K and $T = 7.0$ K are

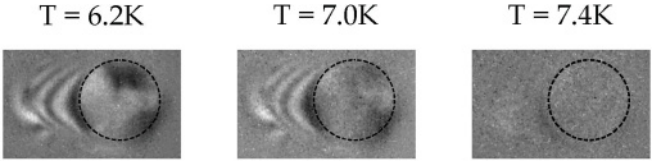

FIG. 7. Meissner phase, sample orientation 90°. Observation of the Meissner effect for a polycrystalline lead sample, $B_{\text{ext}} = 6.4$ mT; black circle indicates the sample (projection diameter =12.7 mm, orientation of B_{ext} perpendicular to the rod axis. Black fringes around the sample are due to spin depolarization caused by the expelled field. For $T = 7.4$ K $> T_c$ fringes disappear. The dark areas inside the circle in the right part of the images ($T = 6.2$ K and 7.0 K) are inhomogeneous trapped magnetic fields that also vanished for $T = 7.4$ K $> T_c$ (see also Fig. 12).

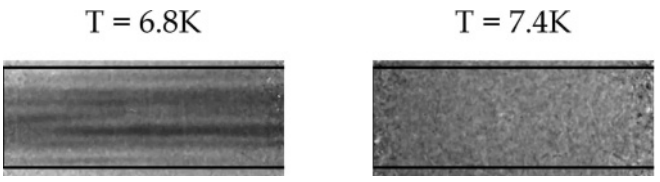

FIG. 8. $B_{ext} = 0$, sample orientation 0°. Observation of flux pinning in the polycrystalline lead sample. Left $T = 6.8$ K, right $T = 7.4$ K ($T_c = 7.19$ K). The fringes in the left image ($T = 6.8$ K) are due to position-dependent depolarization of the neutron spin when it passed through the sample, i.e., one fringe represents all polarized neutrons that underwent the same path integrals $\int B(x,y,z)ds$. Right image: If $T > T_c$ the trapped magnetic field vanished; both images were normalized to the 8 K image (see also Fig. 10). Black lines are 10 mm apart, projection diameter =12.7 mm.

doubtless a hint of trapped magnetic fields because they vanish for $T > T_c$. The magnetic field for this sample in the Meissner phase was similar to the expelled field, as mentioned above, but the fringe structure was much more pronounced in the polycrystalline sample. The magnetic inhomogeneities observed as dark areas in the interior of the lead cylinder were not observed in the crystal sample. Moreover, these fields seemed to depend on the sample temperature, because the image changed from $T = 6.2$ K to $T = 7.0$ K. The change from "dark" to "light" corresponds to a spin rotation of π implying a B field of ∼0.6 mT. In order to investigate a possible intermediate state the sample was rotated in the 0° position (Fig. 8).

Figure 8 shows the measured (normalized) image ($T = 6.8$ K) consisting of a well ordered, nearly parallel fringe system that vanished for $T = 7.4$ K $> T_c$. This fringe system is the result of position-dependent depolarization of the neutron spin due to a trapped magnetic field distribution in the sample.

The fringes in Fig. 8 are located closer to the rod axis than to the edges, contrary to what one would expect for uniform distribution of trapped flux (cf. Figs. 3, 10, and 12). Also, the distance of fringes to each other is constant (both better seen in Fig. 10). A magnetic field in a cylindrical sample causing parallel fringe patterns due to spin rotations cannot be uniform but must have a much different shape, as shown in Fig. 11. Further calculations show that a three-dimensional (3D) spatial distribution consisting of a Gaussian function in the plane perpendicular to the major axis of the cylinder and a nearly constant value of the field along the major axis fit the data best (see below). The field of view (FOV) of the spin analyzer was (unfortunately) once not perfectly homogeneous and then smaller than the magnetic field outside of the sample. A translation of the analyzer (together with its stray field) would have changed the experimental boundary conditions in such a way that the results would not be compatible with previous ones. Therefore in all experimental series nothing was changed except the sample temperature; thus all observations based on these quantum macroscopic effects are due to magnetic fields inside and outside of the sample, only.

The magnetic field distribution outside and inside the sample while in the intermediate state was modeled by 3D functions and path integrals taken over curves within the field distribution yielded the measured fringe pattern. The only boundary condition for all calculations was that the sum of the fields (inside + expelled ones) must not exceed B_{ext}, i.e., if the sample was in the Meissner state (B_{ext} = on, $T < T_c$) the expelled field B_{expel} must be smaller than B_{ext}. Furthermore, if the sample was in the intermediate state, i.e., B_{ext} = off and $T < T_c$, the trapped field B_{trap} must be once smaller than B_{ext} and the sum $B_{trap} + B_{expel}$ must be less or equal B_{ext}. ($B_{trap} + B_{expel} \leqslant B_{ext}$). Another assumption had to be made to explain the measured fringe pattern. If one assumes that B_{ext} homogeneously penetrates the sample, then the magnetic flux is constant for the whole sample and the flux density B_{ext}/dV (dV = small sample volume element) is constant as well. If a certain amount of B_{ext} remains in the sample, say, e.g., $B_{trap} = 0.6B_{ext}$, then B_{expel} must be $0.4B_{ext}$. The amount of B_{trap} was apparently not homogeneously distributed in the sample (as shown by the measured fringe pattern); therefore its profile could not be represented by a constant function.

The solution was to set the $B_{trap} = 0.71B_{ext} = B_{trap,Gauss}$, i.e., equal to the integral of the 2D Gaussian function, which represents the function for B_{trap} in the sample but within a smaller cross section of the y-z plane. Thus the magnetic field was squeezed in such a way that the path integrals became now $V \cdot \int B_{trap,Gauss}(x,y,z)ds$, V being the ratio of the cross section of the cylinder and the reduced cross section of the trapped field. Doing this the calculated images fit nearly perfectly to the measured ones (see Figs. 10 and 12). The best fit function to describe the 3D trapped field was a 3D (normalized) Gaussian function having a FWHM = 4.2(5) mm (the diameter of the sample was 12 mm, the projected measured diameter 12.7 mm). The volume of the cylinder was three-dimensionally scaled with this Gaussian as shown in Fig. 9.

Figure 10 shows the comparison of calculated and imaged field distributions – the calculated image, assuming different trapped fields $B_{trap,}$ and the measured image, at $T = 6.8$ K $< T_c$. Fringe patterns due to neutron spin rotations in the polycrystalline sample being in the intermediate state were observed for temperatures $T < T_c$. Figure 10 shows the image

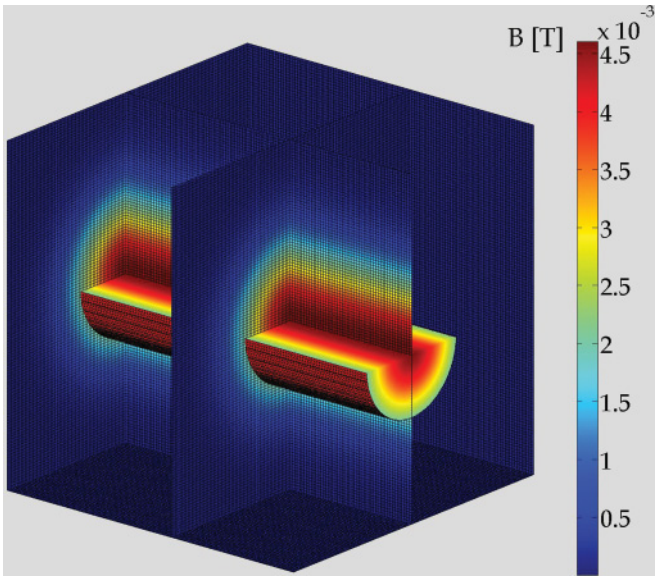

FIG. 9. (Color online) 3D visualization of the trapped magnetic field having a 2D Gaussian shape inside the lead sample (see Fig. 11) which is constant for all points having the same distance to the rod axis.

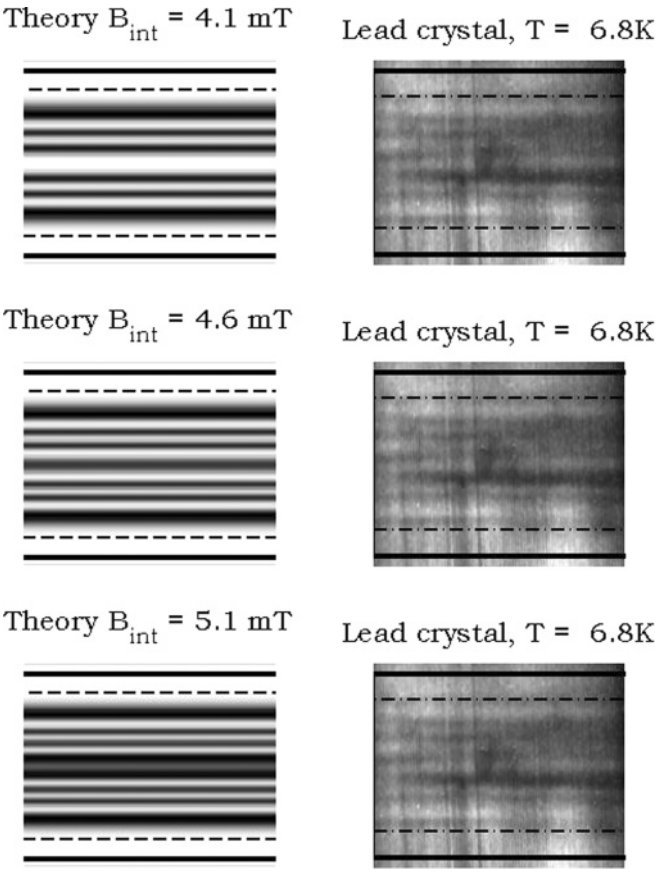

FIG. 10. Calculated and measured fringe pattern due to neutron spin interaction with a trapped magnetic field having Gaussian shape distribution in the y-z plane (cf. Figs. 8 and 11). Solid black lines in the plots indicate the sample cross section; dotted lines delimit the calculated and measured fringe pattern. Best agreement was found for $B_{\text{trap}} = B_{\text{int}} = 4.6$ mT (same figure as Fig. 8, but original rotated 4°).

at $T = 6.8\ \text{K} < T_c$. The best agreement with the calculations was found for $B_{\text{trap}} = B_{\text{int}} = 4.6(5)$ mT. For the fit just two parameters, B_{int} and the FWHM of the Gaussian function, had to be optimized. The dotted lines in plots and images in Fig. 10 compare the spread of the calculated and measured fringes in the sample. Slight variation in the value of the FWHM of the Gaussian function changed the image of the fringes remarkably. The second variable in the fit was the size of the field inside the sample B_{int}, i.e., the trapped field B_{trap}. The boundary condition for B_{trap} was that it must be smaller than B_{ext}. The number and the central part of the calculated fringes were quite sensitive to changes of B_{trap} as shown in Fig. 10; therefore B_{trap} can be given with an accuracy of the order of 50 μT. The trapped magnetic field showed a cross section in the y-z plane as displayed in Fig. 11 which was squeezed to a smaller area in the (y-z) plane. This enhanced B_{trap} for all path integrals close to the rod axis and decreased B_{trap} to the edges of the sample. Therefore we compared the calculated trapped field $B_{\text{trap}} = B_{\text{int}} = 4.6$ mT to be uniform and constant with a squeezed field having a Gaussian shape (Fig. 11). Comparing these calculations with the experimental results (Fig. 10) it is clear that there is a nonuniform flux trapping in the polycrystalline sample.

When the polycrystalline sample was in the Meissner phase only a part of B_{ext} was expelled and part of B_{ext} was trapped.

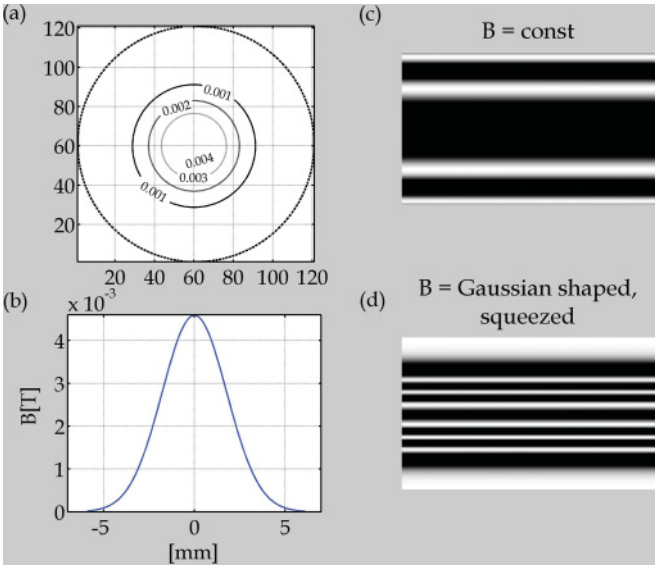

FIG. 11. (Color online) Calculated magnetic field in the polycrystalline lead sample. (a) Cross section of the trapped field in the y-z plane (scale: 120 ≈ 12 mm); dotted (large) circle represents the sample cross section, (b) shape of the field distribution, rod axis at 0 mm. (c) A homogeneous distribution of the trapped field ($B = 4.6 \times 10^{-3}$ T) would have caused this fringe pattern. (d) The measured trapped field distribution of Fig. 10 could be best fitted to the experiment for a squeezed field which had a Gaussian shape of (b) causing the plotted pattern. Image heights in (c) and (d) are 12.7 mm.

Thus, assuming that the expelled field must be less or equal to $B_{\text{ext}} - B_{\text{trap}}$ one had to fit B_{expel} in such a way that it decreased outside the sample. In order to include a certain (measured)

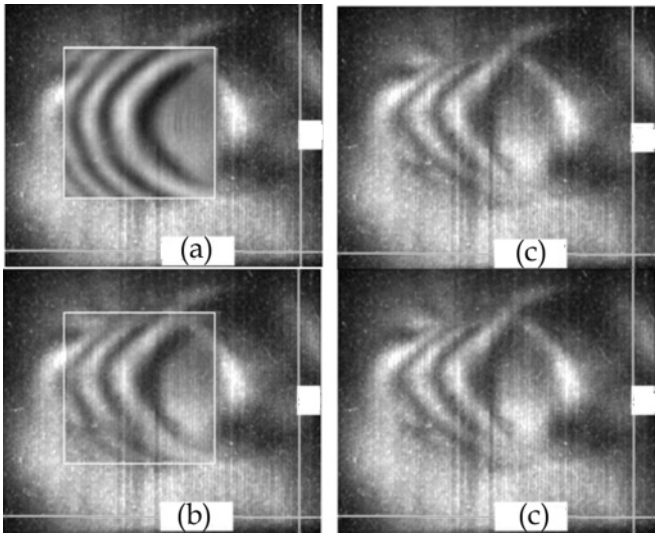

FIG. 12. Partially Meissner effect of a pure, homogeneous polycrystalline lead sample, orientation of the rod axis perpendicular to the external field and perpendicular to the neutron flight direction (misalignment ∼4°). Calculated and measured images overlap: (a) Enhanced part shown in the frame is the calculated image, measured image is damped; (b) measured fringe pattern in the frame is enhanced and calculated is damped; (c) original images (see also Fig. 7). Sizes of the images are 25.8 mm × 21.5 mm.

nonuniformity of B_{ext} due to a small stray field stemming from the spin analyzer (<0.1 mT) and a misalignment of the sample with respect to the neutron flight direction [$\alpha = 4^{\circ}(1)$] the expelled field was fitted to a second (normalized) Gaussian function, having a maximum in the rod axis, but was set at zero at the boundary of the sample. In this way the slope of decrease of the magnetic field ($\sim 1/R$) could be tuned beginning outside at the surface of the sample. The corresponding line integrals were calculated with Eq. (5) setting the angle $\alpha = 90^{\circ} + 4^{\circ}$, the fringe pattern with Eq. (4). Figure 12 shows the comparison of calculated and observed fringe patterns.

The agreement of the calculated with the measured fringe patterns inside and outside of the sample is obvious. Figure 12 shows the full left part but only a small area of the right part of the image due to the reduced field of view of our neutron spin analyzer. The fringe pattern disappeared for $T > T_c$ as is also shown in Figs. 7 and 8.

VI. DISCUSSION

These measurements did not underline assumptions made for trapped or pinned magnetic fields in the single-crystal and polycrystalline samples for $T < T_c$. In the case of a single-crystal lead cylinder one observed the "classical" Meissner effect without any flux pinning or trapping despite the fact of a rather large mosaic spread (1.76°) of the crystal.[34] Such a mosaic spread is connected with a high dislocation density of the order of 10^5–10^7 cm^{-2} (Refs. 35 and 36) and might favor a certain flux pinning which was expected but not verified. From these experimental results one must conclude that for the ⟨110⟩ -single-lead-crystal sample no intermediate state exists.

In the case of the high-purity polycrystalline sample having the same dimensions and shape and being in the Meissner phase, only a part of the applied field was expelled while the rest remained in the sample. Switching off B_{ext}, a certain intermediate state was created, and a squeezed trapped field around the rod axis, observed as an increase in flux density at the center of the cylinder. The trapped magnetic field was not homogeneously distributed in the sample but centered on the rod axis having a Gaussian-like shape and the assumed fields perfectly explained the experimental results. All results described here were uniquely reproducible and allowed the detailed calculations of the trapped and expelled magnetic fields given above. The observed distribution of the magnetic flux might be explained by the so-called Bean model.[37] It is basically derived from the Maxwell equation, $\frac{4\pi}{c} j_c = \nabla \times H$, where j_c is the critical current density that depends on pinning strength. The pinning arises from the spatial variation of the superconducting order parameter. The microscopic regions with magnetic flux tend to occupy the regions with the suppressed order parameter and require a finite force to move them out. Strictly speaking this consideration is also applicable to type II superconductors with well-defined Abrikosov vortices.[38] However, pinning phenomena are quite ubiquitous in moderate κ-type I superconductors, such as bulk lead,[16] and have been visualized on the sample surface using magneto-optical techniques,[9] particularly in bulk lead samples,[16] which was the subject here. In this work we show that it is a true bulk effect. It will be interesting to compare the results of Vélez *et al.*[39] with our technique, because they showed that the geometry of the sample and the direction and amount of the magnetic field lead to certain irreversible features of the intermediate state.

ACKNOWLEDGMENTS

We thank Professor Dr. Ralf Martens-Menzel (Beuth Hochschule für Technik Berlin, Dep. II) and Dr. Nelia Wanderka (Helmholtz Zentrum für Materialien und Energie Berlin) for their detailed analysis of the lead samples. We thank Mr. Charles Strehlow for careful reading of the manuscript. This work was supported by the Federal Ministry of Education and Research (BMBF) Project No 05K10KF1. Work at the Ames Laboratory was supported by the Department of Energy, Basic Energy Sciences under Contract No. DE-AC02-07CH11358.

*treimer@helmholtz-berlin.de

[1] L. Landau, Nature **141**, 688 (1938).
[2] N. V. Sarma and J. R. Moon, Phys. Lett. **24A**, 580 (1967).
[3] A. G. Meshkovsky and A. I. Shalnikov, J. Phys. (USSR) **11**, 1 (1947).
[4] A. G. Meshkovsky and A. I. Shalnikov, J. Exp. Theor. Phys. **17**, 851 (1947).
[5] J. A. Osborn, Phys. Rev. **67**, 351 (1945).
[6] E. H. Brandt, Physica C **332**, 99 (2000).
[7] A. T. Dorsey and R. E. Goldstein, Phys. Rev. B **57**, 3058 (1998).
[8] U. Kunze, B. Lischke, and W. Rodewald, Phys. Status Solidi B **63**, 377 (1974).
[9] R. P. Huebener, *Magnetic Flux Structures of Superconductors*, 2nd ed. (Springer-Verlag, New York, 2001).
[10] A. Fortini and E. Paumier, Phys. Rev. B **14**, 55 (1976).
[11] D. J. E. Callaway, Nucl. Phys. B **344**, 627 (1990).
[12] H. Castro, B. Dutoit, A. Jacquier, M. Baharami, and L. Rinderer, Phys. Rev. B **59**, 596 (1999).
[13] M. J. Van Bael, M. Lange, S. Raedts, V. V. Moshchalkov, A. N. Grigorenko, and S. J. Bending, Phys. Rev. B **68**, 014509 (2003).
[14] A. D. Hernández and D. Domínguez, Phys. Rev. B **72**, 020505 (2005).
[15] J. R. Clem, R. P. Hübner, and D. E. Gallus, J. Low Temp. Phys. **12**, 449 (1973).
[16] R. Prozorov, R. W. Giannetta, A. A. Polyanskii, and G. K. Perkins, Phys. Rev. B **72**, 212508 (2005).
[17] U. Satoshi, S. Jun-ichi, M. Takanori, H. Shigeru, and H. K. Kohji, J. Phys.: Conf. Ser. **43**, 231 (2006).
[18] R. Prozorov and R. W. Gianetta, Supercond. Sci. Technol. **19**, R41 (2006).
[19] R. Prozorov, Phys. Rev. Lett. **98**, 257001 (2007).
[20] J. R. Hoberg and R. Prozorov, Phys. Rev. B **78**, 104511 (2008).
[21] S. Vélez, C. Panadès-Guinart, G. Abril, A. García-Santiago, J. M. Hernandez, and J. Tejada, Phys. Rev. B **78**, 134501 (2008).
[22] R. Prozorov, A. F. Fidler, J. R. Hoberg, and P. C. Canfield, Nat. Phys. **4**, 327 (2008).

[23] J. R. Clem, R. P. Hübner, and D. E. Gallus, J. Low Temp. Phys. **12**, 449 (1973).
[24] G. R. Berdiyorov, A. D. Hernandez, and F. M. Peeters, Phys. Rev. Lett. **103**, 267002 (2009).
[25] W. Treimer, A. Hilger, N. Kardjilov, and M. Strobl, Nucl. Instrum. Methods Phys. Res., Sect. A **542**, 367 (2005).
[26] M. Schulz, A. Neubauer, S. Masalovich, M. Mühlbauer, E. Calzada, B. Schillinger, C. Pfleiderer, and P. Boeni, J. Phys.: Conf. Ser. **211**, 012025 (2010).
[27] M. Schulz, A. Neubauer, M. Mühlbauer, E. Calzada, B. Schillinger, C. Pfleiderer, and P. Böni, J. Phys.: Conf. Ser. **200**, 112009 (2010).
[28] M. Strobl, W. Treimer, P. Walter, S. Keil, and I. Manke, Appl. Phys. Lett. **91**, 254104 (2007).
[29] M. Strobl, C. Grünzweig, A. Hilger, I. Manke, N. Kardjilov, C. David, and F. Pfeiffer, Phys. Rev. Lett. **101**, 123902 (2008).
[30] I. Manke, N. Kardjilov, R. Schäfer, A. Hilger, M. Strobl, M. Dawson, C. Grünzweig, G. Behr, M. Hentschel, C. David, A. Kupsch, A. Lange, and J. Banhart, Nat. Commun. **1**, 125 (2010).
[31] W. Treimer, O. Ebrahimi, N. Karakas, and S. Seidel, Nucl. Instrum. Methods Phys. Res., Sect. A **651**, 53 (2011).
[32] T. Krist, S. J. Kennedy, T. J. Hick, and F. Mezei, Physica B **241–243**, 82 (1998).
[33] N. Kardjilov, I. Manke, M. Strobl, A. Hilger, W. Treimer, M. Meissner, T. Krist, and J. Banhart, Nat. Phys. **4**, 399 (2008).
[34] M. Liesegang, S. Seidel, O. Ebrahimi, N. Karakas, and W. Treimer, BER II Experimental Reports 2009, No. HZB-4, 91, 2010.
[35] J. E. Ayers, J. Cryst. Growth **135**, 71 (1994).
[36] B. Yarlagadda, A. Rodriguez, P. Li, R. Velampati, J. F. Ocampo, E. N. Suarez, P. B. Rago, D. Shah, J. E. Ayers, and F. C. Jain, Appl. Phys. Lett. **92**, 202103 (2008).
[37] C. P. Bean, Rev. Mod. Phys. **36**, 31 (1964).
[38] G. Blatter, M. V. Feigelman, V. B. Geshkenbein, A. I. Larkin, and V. M. Vinokur, Rev. Mod. Phys. **66**, 1125 (1994).
[39] S. Vélez, C. Panadès-Guinart, G. Abril, A. García-Santiago, J. M. Hernandez, and J. Tejada, Phys. Rev. B **78**, 134501 (2008).